RSC Advances

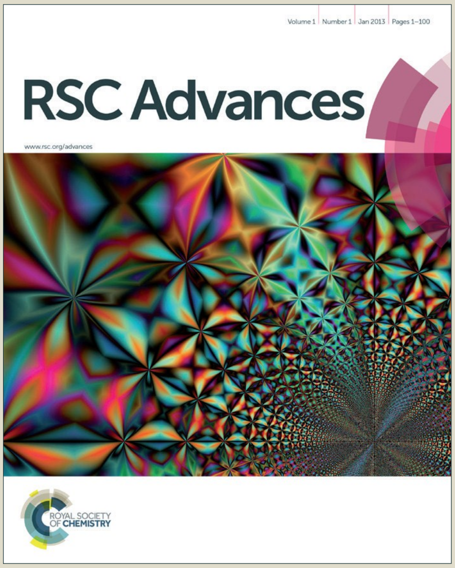

ROYAL SOCIETY
OF **CHEMISTRY**

www.rsc.org/advances

Journal Name

ARTICLE

Rationally Designed Hierarchical MnO_2@NiO Nanostructures for Improved Lithium Ion Storage

Received 00th January 20xx,
Accepted 00th January 20xx

DOI: 10.1039/x0xx00000x

www.rsc.org/

Nana Wang[a], YanjunZhai [a], Xiaojian Ma[a], and Yitai Qian*[a,b]

Designing hierarchical nanostructures used as anodes, involving higher rate capabilities and better cycle lives, to meet further lithium ion batteries applications has attracted wide attention. Herein, a hierarchical core-shell nanostructure MnO_2@NiO with MnO_2 nanorod as a core and NiO flakes as a shell has been synthesized by combining a hydrothermal treatment and an annealing process. MnO_2 nanorods serve as a high theoretical capacity (1233 mAh g^{-1}) material, and allows for efficient electrical and ionic transport owing to its one-dimensional structure. The porous NiO flakes as a shell would enlarge the contact area across the electrode/electrolyte, and can also serve as volume spacers between neighboring MnO_2 nanorods to maintain electrolyte penetration as well as reduce the aggregation during Li^+ insertion/extraction. As a result, such a core-shell structure MnO_2@NiO exhibits improved cycling stability (939 mAh g^{-1} after 200 cycles at the current density of 1 A g^{-1}) and outstanding rate performance, suggesting that the synergetic effect and characteristics of core-shell nanostructure would benefit the electrochemical performance of lithium ion batteries.

Introduction

Lithium ion batteries (LIBs) are regarded as the dominating choice for many applications such as portable, telecommunication equipment and electric vehicles.[1-2] Currently, the commercial graphite used as common anodes but its low capacity (372 mAh g^{-1}) and safety issues cannot keep pace with the rate of progress on new energy economy.[3] Thus, numerous efforts have been devoted to explore alternative anode materials to meet the demand for advanced batteries with high energy density, long lifespan and lightweight design. In this respect, transitional metal oxides (TMOs) have attracted much attention due to their high theoretical capacities which are about two or three times to graphite.[4] Unfortunately, their practical applications are restricted to the poor cycling performances and bad rate properties because of the huge volume variation during Li insertion/extraction.[5]

Enormous strategies have been investigated to overcome the above challenges, involving designing various nanostructures such as nanorods,[6] cubes,[7] tubes,[8] and spheres,[9] because nanostructured electrodes can accommodate the expanded volume caused by repeated Li intercalation/deintercalation and avoid fast capacity decay. Most recently, rational hybridization of two or more active materials have drawn much more attention, because it can make the best use of each material to achieve better LIBs performance by adjusting the morphologies, compositions, and assembling organization of elementary nanobuilding blocks. Especially, hybridized hierarchical nanostructure composites are more attractive owing to the large surface areas and integral configurations, which can not only enlarge the contact area between the electrode and electrolyte, but also provide short and continuous diffusion paths for electron/ion transfer.[10,11] For example, the six-fold-symmetry branched α-Fe_2O_3/SnO_2 nanoheterostructure was prepared by a two-step method, depicts a significantly improved initial discharge capacity of 1167 mA h g^{-1}, which is much better than that of bared SnO_2 nanowires (612 mAh g^{-1}) and α-Fe_2O_3 nanorods (598 mAh g^{-1}), but its cycling stability is not well enough.[12] Branched nanorods of β-MnO_2/α-Fe_2O_3 synthesized by Gu et al. display a reversible capacity of 1028 mAh g^{-1} after 200 cycles, which is also much higher than those of β-MnO_2 nanorods (283 mAh g^{-1}) and porous α-Fe_2O_3 nanorods (314 mAh g^{-1}).[13] Besides, branched Co_3O_4/Fe_2O_3 nanowires also show improved electrochemical properties (cycling stability and good rate performance) compared to their single component Co_3O_4 and Fe_2O_3.[14] Despite those remarkable progresses, TMOs are still far from commercialization. Therefore, continued efforts are still necessary for constructing advanced TMOs electrodes with high power rates and long cycling stability.

As the previous reported, the selected components have great effect on the final performance of hybridized materials.[12-19] Reasonable components will generate excellent properties of electrode materials. MnO_2 is an attractive anode material considering its environmental benignity, natural abundance and highest theoretical capacities among the TMOs (1233 mAh g^{-1}).[13,20] Nevertheless, due to its large volume expansion and low electrical conductivity, individual MnO_2 shows a rapid capacity fading upon galvanostatic cycling.[21] Based on the concept of designed

---

[a] Key Laboratory of Colloid and Interface Chemistry, Ministry of Education, School of Chemistry and Chemical Engineering, Shandong University, Jinan 250100, China. Email: qianyt@sdu.edu.cn.

[b] Hefei National Laboratory for Physical Science at Microscale and Department of Chemistry, University of Science and Technology of China, Hefei, 230026, China

† Electronic Supplementary Information (ESI) available: XRD patterns, TEM, SEM images, BET measurements and CV curves of MnO2 and NiO, See DOI: 10.1039/x0xx00000x

hybridization of active materials into the micro-nano structure, NiO was selected owing to its relative high theoretical capacities (718 mAh g^{-1}) and low toxicity.[20] In particular, NiO shows relatively better capacity retention and cycling stability than MnO_2 presented in previous reports.[22-27] Herein, hierarchical MnO_2@NiO core-shell nanostructures have been successfully constructed via a hydrothermal reaction and then a calcination process. Interestingly, hierarchical MnO_2@NiO core-shell nanostructures presents a nearly two-fold-symmetry and porous NiO flakes are first developed on the surface of MnO_2 nanorods. The porous NiO flakes shell can provide good access of the electrolyte to the electrode surface, reduce ion diffusion lengths and constrain the volume change during cycling.[10] The inner component MnO_2 nanorods can provide high capacity and one dimensional structure could afford continuous electron transfer channels.[11] Benefiting from the advantages of such rationally designed structures, MnO_2@NiO delivers superior electrochemical performance to both individual MnO_2 and NiO. The hierarchical core-shell MnO_2@NiO is characterized by X-ray diffraction (XRD) patterns, scanning electron microscopy (SEM) images, transmission electron microscopy (TEM) images and high-resolution TEM (HRTEM) images.

Experimental section

Synthesis of MnOOH: the synthesis of MnOOH nanorods was modified from previous report.[28] Briefly, potassium permanganate ($KMnO_4$, 0.1 g) and polyethylene glycol 400 (2 mL) were dissolved in deionized water (40 mL) under magnetic stirring. After stirred for 30 min, the resulting solution was transferred into Teflon-lined autoclave and then heated to 160 °C for 5 h. The product was collected by centrifugation and washed with deionized water and ethanol for three times.

Synthesis of MnO2@NiO: The obtained MnOOH nanorods (0.05 g) were redispersed into 20 mL ethanol and sonicated for 30 min to assure the good dispersity. Then, 1.5 mmol of $Ni(NO_3)_2{\cdot}6H_2O$ and 3 mmol of urea were dissolved into 20 mL deionized water. The above two solutions were then mixed and transferred into Teflon-lined autoclave. After heated to 120 °C for 6 h, the product MnOOH@$Ni_2CO_3(OH)_2{\cdot}2H_2O$ was collected and washed with deionized water. Afterwards, annealing the MnOOH@$Ni_2CO_3(OH)_2{\cdot}2H_2O$ under air at 400 °C for 2 h to obtain MnO_2@NiO.

Sample Characterization: X-ray powder diffraction (XRD) patterns were collected on a Bruker D8 advanced X-ray diffractometer using CuK_α radiation. The morphology of the as-prepared nanostructures was obtained from a transmission electron microscope (JEOL JEM 1011) and a field-emission scanning electron microscope (SUPRA^{TM}55). HRTEM images were achieved with an analytic transmission electron microscopy (JEOL-2100). Nitrogen sorption isotherms were recorded on a Micromeritics ASAP-2020HD88 instrument. Inductive Coupled Plasma Atomic Emission Spectrometer (ICP-AES, IRIS Inrtrepid II XSP) was used to analyze the chemical composition.

Electrochemical measurements: The working electrode is consisted of active material, conductive carbon black and sodium salt of caboxymethyl cellulose (CMC) in a weight ratio of 70: 20: 10. The materials were dispersed in water and milled for 30 minutes to form homogenous slurry. The slurry was then pasted onto copper foil and then dried at 60 °C for 12 h under vacuum. The typical mass loading of the active material was in the range of 1.5 - 2 mg cm^{-1}. CR2032-type coin cells were assembled in an argon filled glovebox (Mikrouna, Super 1220/750/900) with a Celgard 2400 membrane used as the separator and Li-metal circular foil as the reference/counter electrode. The used electrolyte consists of 1 M $LiPF_6$ dissolved into a mixture of diethyl carbonate (DEC), dimethyl carbonate (DMC) and ethylene carbonate (EC) (1:1:1, vol. ratio). Galvanostatic charge-discharge tests were performed on Land-CT2001A battery cyclers (Wuhan, China). Cyclic voltammograms (CV) profiles were measured by LK2005A electrochemical workstation (Tianjin China). Electrochemical impedance spectra (EIS) were recorded on an electrochemical workstation (AUTOLAB PGSTAT204).

Results and discussion

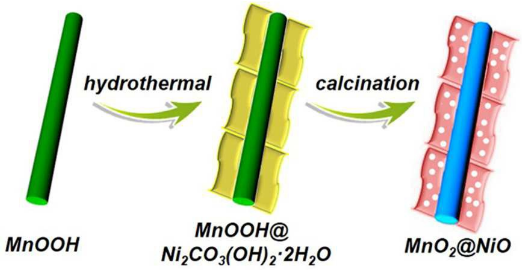

Scheme 1. Schematic illustration of the synthetic process of hierarchical MnO_2@NiO core-shell nanostructures.

The synthesis procedure of hierarchical MnO_2@NiO core-shell nanostructures involves three steps as summarized in Scheme 1. First, uniform MnOOH nanorods prepared by a hydrothermal method possess a mean diameter of 100 nm and length of 5 µm (Figure S1). Second, the MnOOH nanorods can serve as backbones to support the subsequent growth of $Ni(NO_3)_2{\cdot}6H_2O$ nanostructures through a facile hydrothermal reaction, because of abundant oxhydryl groups anchored on the surface of MnOOH which promote the subsequent coating. Finally, the obtained precursors MnOOH@ $Ni_2CO_3(OH)_2{\cdot}2H_2O$ were annealed in air, leading to the formation of hierarchical MnO_2@NiO core-shell nanostructures.

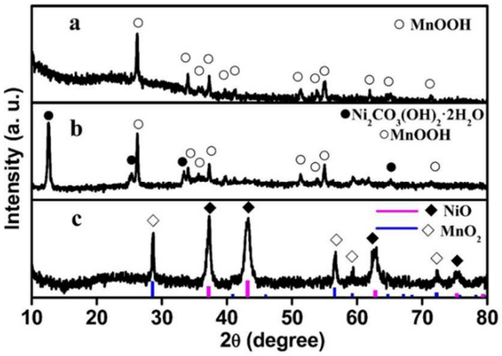

Figure 1. XRD patterns of a) MnOOH nanorods, b) the precursor MnOOH@$Ni_2CO_3(OH)_2{\cdot}2H_2O$, c) hierarchical MnO_2@NiO core-shell nanostructures. The referential JCPDS card spectra for MnO_2 and NiO are shown in the bottom.

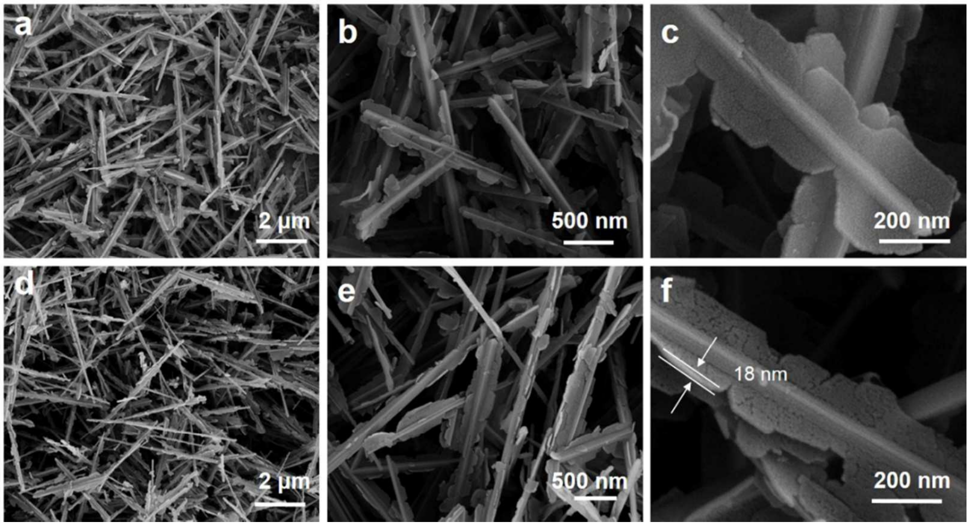

Figure 2. SEM images of (a-c) the precursors, (d-f) hierarchical MnO_2@NiO core-shell nanostructures.

Figure 1 shows the XRD patterns of the samples recorded at different stage to verify the compositional transformation. In Figure 1a, all the diffraction peaks can be assigned to monoclinic MnOOH (JCPDS card no. 41-1379). The XRD patterns (Figure 1b) of the precursor obtained via hydrothermal reaction can be indexed to orthorhombic $Ni_2CO_3(OH)_2{\cdot}2H_2O$ (JCPDS card no. 29-0868) accompany with MnOOH.[29] After annealing in air atmosphere, the precursor was completely transformed into tetraganol phase β-MnO_2 (JCPDS card no. 24-0735) and cube phase NiO (JCPDS card no. 47-1049).

Figure 2 shows the typical SEM images of the as-prepared products. The low-magnification SEM images (Figure 2a and 2b) indicate that the precursors exhibit hierarchical structures with numerous flakes grown on the surface of MnOOH nanorods. Interestingly, the height of these flakes is discontinuous but their thickness is similar (~ 18 nm, Figure 2c). The hierarchical structure exhibits a two-fold-symmetry while the angle of 180^{o} between adjoining flakes. After the annealing process, the morphology of the product is basically maintained (Figure 2d and 2e), indicating that the hierarchical structures exhibit good thermal stability. However, it is clearly observed that the surface of NiO flakes becomes rough and highly porous due to the release of gases (CO_2, H_2O etc.) (Figure 2f). Such porous shell offers important merits of the hierarchical MnO_2@NiO core-shell nanostructures including larger interfacial area and more reactive sites which facilitate charge transfer and reduce the diffusion length of ion and electron. These properties promise this material to deserve higher rate capabilities and better cycle lives.[10]

Figure 3 displays the TEM and HRTEM characterization of the hierarchical MnO_2@NiO structures. The TEM images (Figure 3a and 3b) confirms the core-shell structure by the contrast light and dark areas. As pointed by the white lines, it is clearly observed that the height of NiO flakes is about 50 nm, and it can be also revealed that NiO flakes are highly porous. HRTEM images provide lattice fringes with their spacing about 0.24 nm and 0.21 nm, corresponding to (101) planes of MnO_2 and (200) planes of NiO (Figure 3c and 3d). The chemical composition has been tested by ICP-AES technique, showing an atomic Mn/Ni ratio of 3.7: 1 which is in consistent with EDX spectra (Figure S2).

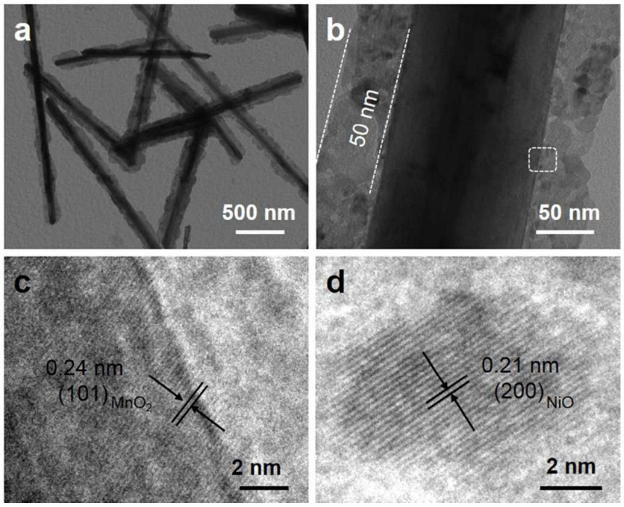

Figure 3. (a,b) TEM images and (c,d) HRTEM images of hierarchical MnO_2@NiO core-shell nanostructures.

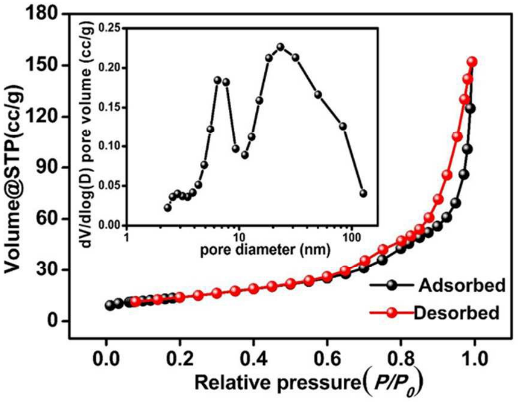

Figure 4. Nitrogen adsorption/desorption isotherms and the corresponding pore size distribution (inset) of hierarchical MnO_2@NiO core-shell nanostructures.

Nitrogen sorption isotherms and pore size distribution were provided to investigate the porous properties of hierarchical MnO_2@NiO core-shell nanostructures and shown in Figure 4. The isotherm of MnO_2@NiO can be classified as Type IV with an obvious Type H1 hysteresis loop, indicating the mesoporous characteristic ofmaterials.[30] The Brunauer-Emmett-Teller (BET) specific surface area and pore volumes of MnO_2@NiO are 59.3 m^2 g^{-1} and 0.3 cm^3 g^{-1}, respectively. The pore size distributions, calculated from the adsorption isotherms, have two wide peaks centered at ~ 7 nm and ~ 24 nm. The nitrogen sorption isotherms of MnO_2 naorods is shown in Figure S4, where type III isotherms can be detected, demonstrating the nonporous feature of the sample.[30] This is consistent with the enlarged TEM images of MnO_2 (Figure 3b and Figure S3). After introduction of porous NiO flakes, the surface area of the composite increased remarkably (Figure 4 and Figure S5), which will benefit the electrochemical properties of composite because this can enlarge the contact area between electrolyte and electrode and provide buffer zone for volume variation by the pores.[10]

The electrochemical performances of MnO_2@NiO such as CVs, specific capacities, long cycling stability and rate property were systematic studied. Figure 5a demonstrates the first five CV curves of MnO_2@NiO as an anode material using Li foil as the reference and counter electrode. Four cathodic peaks in the first cycle are observed. The weak peak at 0.71 V can be ascribed to the electrolyte decomposition forming the solid-electrolyte interface (SEI) layer and vanished in the following cycles.[31] The peaks located at 0.96 V and 0.25 V may be attributed to the reduction of MnO_2 to Mn^{2+} and Mn^{2+} to metal Mn, respectively.[13,26] The intense peak centered at 0.50 V is due to the reduction of NiO to metal Ni.[32,33] In the subsequent cycles, the main reduction peaks changed to 1.01 V and 0.29 V because of the structure rearrangement after first cycle.[34,35] The anodic peaks at 1.29 V is assigned to oxidation of metal Mn to Mn^{2+}. The peak at 2.08 V is caused by oxidation of Mn^{2+} and Ni to MnO_2 and NiO, respectively.[13,33] It is worth noting that the CV peaks of MnO_2@NiO during the anodic processes overlap very well in comparison to pure MnO_2 and NiO (Figure S7), indicating that the metal Ni (or Ni^{2+}) and Mn^{2+} can facilitate the sufficient oxidation on each other. Thus, the cycling performance of MnO_2@NiO would be enhanced contrast to individual MnO_2 and NiO.

Figure 5b displays the first discharge-charge profiles of MnO_2 nanorods, NiO nanoflowers and hierarchical MnO_2@NiO core-shell nanostructures at a current density of 1 A g^{-1} in the range of 0.01 – 3.0 V. The discharge/charge curves of the MnO_2@NiO core-shell nanostructures can be considered as a blend of β-MnO_2 and NiO, which also agrees with CV examination. MnO_2@NiO core-shell nanostructures exhibit discharge capacity of 1495 mAh g^{-1} and charge capacity of 1150 mAh g^{-1}, corresponding to an initial capacity loss of 23.1%, which is better than that of MnO_2 nanorods (41.2%) and NiO naonflowers (27.8%). The improved performance may be attributed to the synergetic effect of those components, which is consistent to the CV measurement. The first cycle capacities are higher than their theoretical capacities (MnO_2: 1233 mAh g^{-1}. NiO: 718 mAh g^{-1}. MnO_2@NiO (81.3 wt% MnO_2, 18.7 wt% NiO): 1135 mAh g^{-1}), which might arise from electrolyte decomposition, interfacial storage and lithium ions into acetylene black, and is common in TMOs electrodes.[36-39]

The cycling performance of MnO_2@NiO core-shell nanostructures is shown in Figure 5c. After 200 cycles, the sample still can maintain 939 mAh g^{-1} at the high current density of 1 A g^{-1}, which is much better than that of single MnO_2 naorods (134 mAh g^{-1}) and NiO naoflowers (402 mAh g^{-1}) under the same condition. Moreover, the coulombic efficiency for MnO_2@NiO maintains above 98% after the initial cycle. This phenomenon can be also discovered in other hierarchical hybridized materials because the hybridization can take full advantage of the primary nanobuilding blocks by controlling their morphologies, compositions, and assembling organization. In addition, the important rate performance was also studied and depicted in Figure 5d, the MnO_2@NiO core-shell nanostructures show 1170, 1210, 1020, 920, 650, and 420, mAh g^{-1} at the corresponding current densities of 0.05, 0.2, 0.5, 1, 2, and 4 A g^{-1}, which is superior to that of single MnO_2 nanorods (970, 750, 550, 290, 90, and 46 mAh g^{-1}) and NiO naoflowers (540, 345, 171, 60, 28, and 8.7 mAh g^{-1}) in the same circumstances. It is noted that the specific capacity of MnO_2@NiO still retains at 420 mAh g^{-1} even at the high rate of 4 A g^{-1}, which is much higher than MnO_2 nanorods (46 mAh g^{-1}) and NiO (8.7 mAh g^{-1}). More importantly, after high rate charge/discharge, the capacity of the MnO_2@NiO core-shell nanostructures (1180 mAh g^{-1}) is recovered when the current density was back to 0.05 A g^{-1}, indicating their good structure stability. However, the capacities of MnO_2 and NiO could not be recovered completely after testing at higher rates. The superior rate performance and cycling stability made MnO_2@NiO core-shell nanostructures as a very promising candidate for LIBs applications.

Electrochemical impedance spectroscopy (EIS) measurements were studied to further explain the excellent electrochemical performance of MnO_2@NiO (Figure 6a). Nyquist plots consist a sloping line in the low frequency region ascribed to mass transfer process, and a semicircle in the high frequency attributed to the charge transfer impedance.[17] The fitting equivalent electrical circuit is analyzed shown inset of Figure 6a. The charge transfer resistance of NiO (67 Ω) and MnO_2@NiO (89 Ω) are much lower than MnO_2 (217 Ω), indicating an improved conductivity. Simultaneously, NiO and MnO_2@NiO display more vertical straight lines compared to MnO_2, implying the faster Li-ion diffusion behavior. These results indicate that the

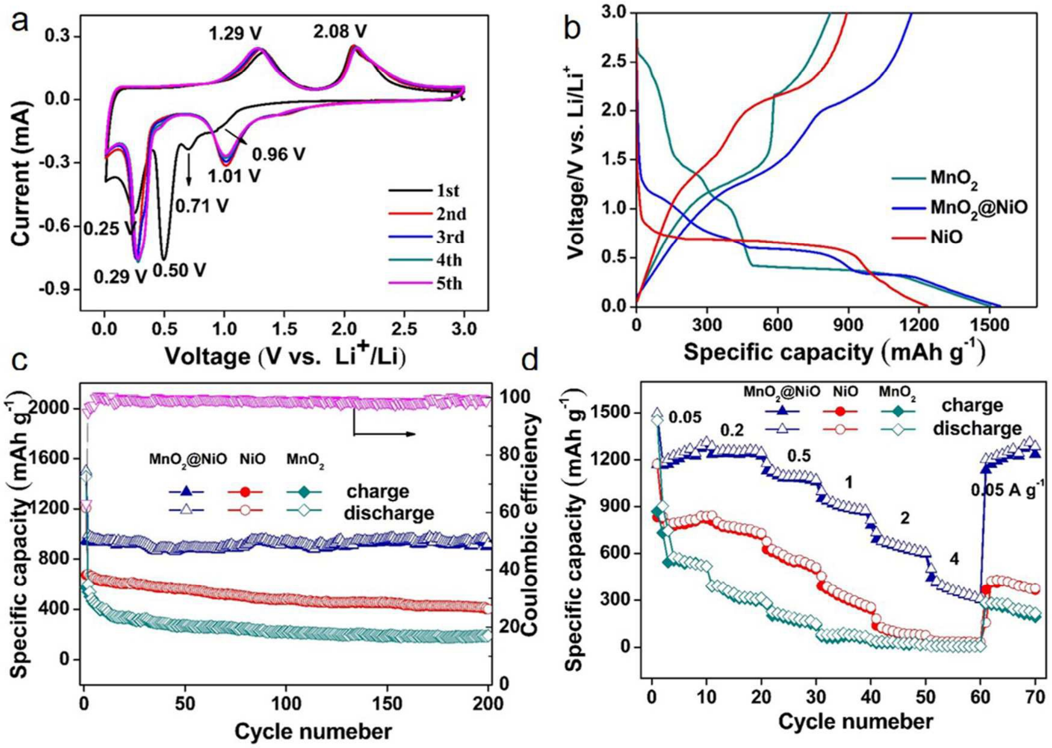

Figure 5. (a) CV curves of the MnO_2@NiO electrode at a scanning rate of 0.1 mV s^{-1} in the range of 0.01 – 3 V. (b) First discharge-charge curves at a current density of 1 A g^{-1} and (c) cycling performance at a current density of 1 A g^{-1} and (d) cycling performance at various current rates of pure MnO_2, NiO and hierarchical MnO_2@NiO core-shell nanostructures. Coulombic efficiency for MnO_2@NiO was provided in Figure 5(c).

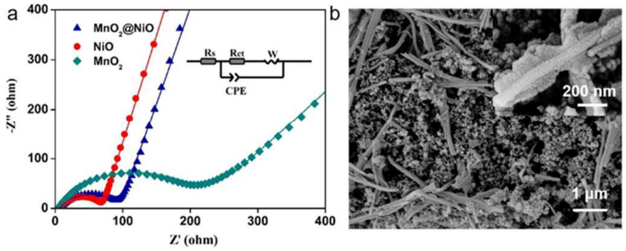

Figure 6. (a) Nyquist plots for the electrodes based on MnO_2, NiO and MnO_2@NiO after 5 cycles at the same voltage of 2.8 V during charge process. The figure inseted is the equivalent circuit to fit the plots. (b) Low and high magnification SEM images of MnO_2@NiO electrode after 20 cycles.

combination of MnO_2 with NiO can improve the ion diffusion and charge transfer distinctly, which would take full advantage of the high theoretical capacity of MnO_2. Figure 6b demonstrates SEM images of the MnO_2@NiO electrode after 20 cycles at the current density of 1 A g^{-1}. The hierarchical structures can be still maintained while MnO_2 nanorods curved at a certain extent due to the repeated lithiation/delithiation, implying that one dimensional structure can effectively buffer the volume expansion. Furthermore, the NiO flakes were still tightly connected to the surface of MnO_2 nanorods without structure collapse, promising the outstanding structural stability.

The improved electrochemical properties involving high rate capability and excellent cycle performance can be ascribed to the rationally designed hierarchical structure and synergistic effects of MnO_2 and NiO. First, abundant pores extend the electrodes /electrolyte contact area and reduce path lengths for electron/ion diffusion, promising increased utilization of active materials. Meanwhile, MnO_2@NiO exhibits the better conductivity and faster Li-ion diffusion behavior. Furthermore, MnO_2 and NiO promote each other’s sufficient reaction with Li/Li^+, enabling the high capacity without reduction. Last, plentiful free spaces between the flakes help accommodate severe volume changes during cycling, avoid disintegration as well as aggregation of components and ensure the structure integrity after long cycling. Thus, the high capacity along with better cycling stability of the electrodes were obtained.

Conclusion

The hierarchical MnO_2@NiO core-shell nanostructures were successfully synthesized via hydrothermal growth of NiO precursor flakes on MnOOH nanorods, presenting a near two-fold symmetry. BET measurements and TEM images indicate that the main pores almost on the NiO flakes due to the decomposition of the precursor. CVs and EIS tests confirm that the synergetic effect promote electrical conductivity, charge transfer and ion diffusion. Such a hierarchical structure demonstrates the lower initial irreversible capacities loss and maintains 939 mAh g^{-1} after 200 cycles at a current density of 1 A g^{-1}. The electrochemical performance of the complex structures is better than both single component which can also be attributed to the heterostructures. The superior rate performance and cycling stability made hierarchical MnO_2@NiO core-shell nanostructures a very promising candidate for LIBs applications.

Acknowledgements

This work was supported by the 973 Project of China (No. 2011CB935901), the National Nature Science Foundation of China (No. 91022033, 51172076 and 21471090), Shandong Provincial Natural Science Foundation for Distinguished Young Scholar (JQ201205), Independent Innovation Foundations of Shandong University (2012ZD007), and new-faculty start-up funding in Shandong University.

Notes and references

1 J. M. Tarascon and M. Armand, *Nature*, 2001, **414**, 359.
2 M. Armand and J. M. Tarascon, *Nature*, 2008, **458,** 652.
3 Y. Idota, T. Kubota, A. Matsufuji, Y. Maekawa and T. Miyasaka, *Science*, 1997, **276**, 1395.
4 P. Poizot, S. Laruelle, S. Grugeon, L. Dupont and J. M. Tarascon, *Nature,* 2000, **407**, 496.
5 H. L Wang, L. F. Cui, Y. Y, H. S. Casalongue, J. T. Robinson, Y. Y. Liang, Y. Cui and H. J. Dai, *J. Am. Chem. Soc.*, 2010, **132**, 13978.
6 Z. C. Bai, N. Fan, C. H. Sun, Z. C. Ju, C. L. Guo, J. Yang and Y. T. Qian, *Nanoscale*, 2013, **5**, 2442.
7 A. Rong, X. P. Gao, G. R. Li, T. Y. Yan, H. Y. Zhu, J. Q. Qu and D. Y. Song, *J. Phys. Chem. B*, 2006, **110**, 14754.
8 Z. C. Bai, N. Fan, Z. C. Ju, C. L. Guo, Y. T. Qian, B. Tang and S. L. Xiong, *J. Mater. Chem. A*, 2013, **1**, 10985.
9 N. N. Wang, X. J. Ma, H. Y. Xu, L. Chen, J. Yue, F. E. Niu, J. Yang and Y. T. Qian, *Nano Energy*, 2014, **6**, 193.
10 A. Vu, Y.Q. Qian, A. Stein, *Adv. Energy Mater.*, 2012, **2**, 1056.
11 J. Y. Huang, L. Zhong, C. M. Wang, J. P. Sullivan, W. Xu, L. Q. Zhang, S. X. Mao, N. S. Hudak, X. H. Liu, A. Subramanian, H. Y. Fan, L. Qi, A. Kushima and J. Li, *Science*, 2010, **330**, 1515.
12 W. W. Zhou, C. W. Cheng, J. P. Liu, Y. Y. Tay, J. Jiang, X. T. Jia, J. X. Zhang, H. Gong, H. H. Hng, T. Yu and H. J. Fan, *Adv. Funct. Mater.*, 2011, **21**, 2439.
13 X. Gu, L. Chen, Z. C. Ju, H. Y. Xu, J. Yang and Y. T. Qian, *Adv. Funct. Mater.*, 2013, **23**, 4049.
14 H. Wu, M. Xu, Y. C. Wang and G. F. Zheng, Nano Res., 2013, **6**, 167.
15 Y. S. Luo, J. S. Luo, J. Jiang, W. W. Zhou, H. P. Yang, X. Y. Qi, H. Zhang, H. J. Fan, D. Y. W. Yu, C. M. Li and T. Yu, *Energy Environ. Sci.*, 2012, **5**, 6559.
16 Y. P. Tang, D. Q. Wu, S. Chen, F. Zhang, J. P. Jia and X. L. Feng, *Energy Environ. Sci.*, 2013, **6**, 2447.
17 J. S. Luo, X. H. Xia, Y. S. Luo, C. Guan, J. L. Liu, X. Y. Qi, C. F. Ng, T. Y, H. Zhang, H. J. Fan, *Adv. Energy Mater.*, 2013, **3**, 737.
18 D. W. Kim, I. S. Hwang, S. J. Kwon, H. Y. Kang, K. S. Park, Y. J. Choi, K. J. Choi and J. G. Park, *Nano Lett.*, 2007, **7**, 3040.
19 C. R. Zhu, X. H. Xia, J. L. Liu, Z. X. Fan, D. L. Dong, H. Zhang, H. J. Fan, *Nano Energy*, 2014, **4**, 105.
20 B. J. Cabana, L. Monconduit, D. Larcher and M. R. Palacín, *Adv. Mater.*, 2010, **22**, E170.
21 J. Desilvestro and O. Haas, *J. Electrochem. Soc.*, 1990, **137**, 5C.
22 X. H. Huang, J. P. Tu, X. H. Xia, X. L. Wang, J. Y. Xiang, L. Zhang and Y. Zhou, *J. Power Sources*, 2009, **188**, 588.
23 X. H. Huang, J. P. Tu, X. H. Xia, X. L. Wang, J. Y. Xiang, *Electrochem. Commun.*, 2008, **10**, 1288.
24 X. L. Sun, C. L. Yan, Y. Chen, W. P. Si, J. W. Deng, S. Oswald, L. F. Liu and O. G. Schmidt, *Adv. Energy Mater.*, 2014, DOI: 10.1002/aenm.201300912.
25 A. L. M. Reddy, M. M. Shaijumon, S. R. Gowda and P. M. Ajayan, *Nano Lett.*, 2009, **9**, 1002.
26 H. Xia, M. Lai and L. Lu, *J. Mater. Chem.*, 2010, **20**, 6896.
27 J. M. Kim, Y. S. Huh, Y. K. Han, M. S. Cho and H. J. Kim, *Electrochem. Commun.*, 2012, 14, 32.
28 Z. C. Bai, B. Sun, N. Fan, Z. C. Ju, M. H. Li, L. Q. Xu and Y. T. Qian, *Chem. Eur. J.*, 2012, **18**, 5319.
29 G. Q. Zhang, L. Yu, H. E. Hoster and X. W. Lou, *Nanoscale*, 2013, **5**, 877.
30 M. Kruk and M. Jaroniec, *Chem. Mater.*, 2001, **13**, 3169-3183.
31 S. Grugeon, S. Laruelle, R. Herrera-Urbina, L. Dupont P. Poizot, and J. M. Tarascon, *J. Electrochem. Soc.*, 2001, **148**, A285.
32 Y. F. Yuan, X. H. Xia, J. B. Wu, J. L. Yang, Y. B. Chen and S. Y. Guo, *Electrochem. Commun.*, 2010, **12**, 890.
33 N. N Wang, L. Chen, X. J. Ma, J. Yue, F. E. Niu, H. Y. Xu, J. Yang and Y. T. Qian, *J. Mater. Chem. A*, 2014, **2**, 16847.
34 G. Binotto, D. Larcher, A.S. Prakash, R. H-Urbina, M. S. Hegde and J. M. Tarascon, *Chem. Mater.*, 2007, **19**, 3032.
35 Z. C. Bai, Z. C. Ju, C. L. Guo, Y. T. Qian, B. Tang and S. L. Xiong, *Nanoscale*, 2014, **6**, 3268.
36 A. Ponrouch, P. L. Taberna, P. Simon and M. R. Palacín, *Electrochim. Acta*, 2012, **61**, 13.
37 Y. F. Zhukovskii, P. Balaya, E. A. Kotomin and J. Maier, *Phys. Rev. Lett.*, 2006, **96**, 058302.
38 Z. C. Bai, Y. H. Zhang, Y. W. Zhang, C. L. Guo, B. Tang and D. Sun, *J. Mater. Chem. A,* 2015, 3, 5266.
39 Z. C. Bai, X. Y. Zhang, Y. W. Zhang, C. L. Guo and B. Tang, *J. Mater. Chem. A,* 2014, 2, 16755.